Electronic Supplementary Material (ESI) for Journal of Materials Chemistry A.

Supplementary Information for

# Self-floating maize straw/graphene aerogel synthesized based on microbubble and ice crystal templates for efficient solar-driven interfacial water evaporation

Yan Kong,[a] Hongbing Dan,[a] Wenjia Kong,[a] Yue Gao,*[a] Yanan Shang,[a] Kaidi Ji,[a] Qinyan Yue*[a] and Baoyu Gao [a]

a. Shandong Key Laboratory of Water Pollution Control and Resource Reuse, School of Environmental Science and Engineering, Shandong University, Qingdao 266200, PR China

**This supplement contains:**

Experimental Section

Supplemental Video S1-S4

Supplemental Figure S1-S7

Supplemental Table S1-S3

Supplemental References

## 1. Experimental Section

### 1.1 Materials

The maize straws used in the experiment were collected from farmland after being harvested in Shandong province of China. The maize straw was washed and dried for 24 hours and kept at 70°C in a drying cabinet, then crushed by a grinder and sieved to 100 mesh for subsequent experiments. Sodium chlorite (SC), urea, hydrogen peroxide ($H_2O_2$), hydrochloric acid (HCl), sulfuric acid ($H_2SO_4$), phosphoric acid ($H_3PO_4$), L-ascorbic acid, acetic acid, potassium permanganate ($KMnO_4$), and Sodium dodecyl sulfate (SDS) were purchased from Sinopharm Chemical Reagent Co., Ltd. (Shanghai, China). Flake graphite was purchased from Jinrilai Carbon Reagents Co., Ltd. (Qingdao, China).

### 1.2 Preparation of Graphene oxide (GO) and pretreatment of maize straw

GO was synthesized by the oxidation of Graphite powder according to the modified Hummer's method: in brief, 3.0 g graphite powder, 18.0 g $KMnO_4$ and a mixture of concentrated $H_2SO_4$ and $H_3PO_4$ (V: V =360:40) were placed in a flask and stirred magnetically. The mixture was heated to 50 $^{o}$C and kept at this temperature for 12 h. Then the reaction was cooled to room temperature and poured onto ice with $H_2O_2$ (30%, 3 mL). The mixture was filtered and washed with 200 mL of water, 200 mL of 30% HCl and 200 mL of ethanol, respectively. Finally, the GO was obtained by drying in vacuum at 60 $^{o}$C for 24 h. The graphene oxide solution was crushed by an ultrasonic breaker for 5 minutes to become a homogeneous solution.

10 g of sodium chlorite was dissolved in 1000 mL of ultrapure water, and the pH of the sodium chlorite solution was adjusted to 4.5 with acetic acid. 20g of maize straw was added to the sodium chlorite solution and stirred at 1000 rpm and kept at 80°C for 2h. Wash with deionized water until milky white, and dry to obtain pretreated maize straw.

### 1.3 Preparation of 3D-maize straw/GO aerogel and nitrogen-doped GO/ maize straw aerogel

Take a certain amount of graphene solution (5mg/mL) and pretreated straw (5mg/mL) and mix well, then add 2mL sodium dodecyl sulfate (50mg/mL) and 0.5g ascorbic acid. The foam was rapidly stirred for 5 minutes at 1600 rpm with a mechanical stirrer. Pour into the mold and move to an oven at 75°C for 1 hour for pre-reduction, then move to a -20°C low-temperature refrigerator for 6 hours to complete pre-freezing, after taking it out, place it in an oven at 95°C and heat for 4 hours for further reduction and self-assembly. The obtained hydrogel was soaked in ultra-pure water and soaked in alcohol to remove the unreacted substance. Finally, the hydrogel was placed in a blast oven and dried for 1 hour to obtain 3D-maize straw/graphene aerogel. The volume ratio of the maize straw uniform solution to the graphene oxide solution is 5:1, 2:1, 1:1, 0.5:1,0.2:1, 0:1 and the prepared maize straw/GO aerogels are named GM1, GM2, GM3, GM4, GM5, and GM0, respectively.

For nitrogen-doped maize straw/GO aerogel, after adding maize straw and graphene, add an appropriate amount of urea, the other preparation processes are the same as 3D-maize straw/GO aerogel, in which the amount of urea added is 0, 0.25g, 0.5g, 0.75g, 1g, 2g, and the prepared nitrogen-doped maize straw/GO aerogels are named GMN0 (GM4), GMN1, GMN2, GMN3, GMN4, GMN5, respectively.

### 1.4 Characterization

The surface morphology of maize straw/GO aerogel and nitrogen-doped maize straw/GO aerogel was characterized by scanning electron microscopy (SEM, Hitachi, SU8010). Hydrophilicity and hydrophobicity were measured by a contact angle analyzer (KSV CM20, Finland) at room temperature. The interaction between maize straw, graphene and nitrogen atoms was measured by Raman spectroscopy system (2000, Renishaw) with spectrum scanned from 50 to 1800 cm$^{-1}$, Fourier-transform infrared (FTIR) spectrometer (ThermoFisher, Nicolet 5700) with spectrum scanned from 4000 to 650 cm$^{-1}$, and XPS spectrometer (ThermoFisher, ESCALAB 250XI) in the range of 0-1350 eV. The thermal behavior was measured by thermogravimetric analysis (TGA-50 analyzer), under a nitrogen purge of 100 mL min$^{-1}$, and the aerogel was heated from 25 to 800 C at 10 C min$^{-1}$. The absorption spectrum of sunlight of an aerogel was recorded using a UV-Vis-NIR spectrophotometer with an integrating sphere (PerkinElmer, USA). The infrared imaging of aerogels under solar radiation was captured using an infrared camera (ST9450, Xima, Hong Kong). The thermal conductivity measurement of GM0, GM4 and, GMN2 was performed on a thermal conductivity tester ((Hot Disk TPS 2500S).

### 1.4 Solar steam generation test

A cylindrical maize straw/GO aerogel with a diameter of 2 cm was floated in a 100 mL beaker. In order to reduce the experimental error caused by the evaporation of bulk of water that is covered by the aerogel, a hollow polystyrene foam ring was placed in the outer ring of the aerogel to protect the water from exposure. The simulated solar radiation is provided by a xenon lamp system (CEL-HXF300, $\lambda > 460$ nm) with an AM 1.5 G filter, and the beaker filled with seawater or emulsified oil is placed on a computer-connected electronic balance (accuracy 0.1 mg), real-time recording weight loss. The infrared imaging of aerogels under solar radiation was captured using an infrared camera (ST9450, Xima, Hong Kong). The ambient temperature is about 25°C and the humidity is about 50% during the measurement period. The 3D-EEM spectrum was detected to determine the natural organic matter in water using luminescence spectroscopy (F-4500, Hitachi, Japan). The anions and cations in seawater were measured by ion chromatography (CIC-D100, ShengHan, China). 1 g silicone oil and 0.1 g Span80 were added into 100 mL deionized water and stirred vigorously for 24 hours to obtain the stabilized oil-in-water emulsion. Optical images of emulsified oil and recovered water were taken with a polarizing microscope (Nikon, ECLIPSE LV100POL). The evaporation rate was calculated using the following equation (1):

$$m = \Delta m/(S \times t) \tag{1}$$

where $m$ (kg $m^{-2}$ $h^{-1}$) is the evaporation rate, $\Delta m$ is the mass change in 1 h (kg), $S$ is the area of the aerogel ($m^2$)

### 1.5 Calculation of equivalent evaporation enthalpy

According to previous reports in the literature, the equivalent enthalpy of evaporation is calculated through the following experiment. The water and aerogels with the same surface area were controlled in a closed container at the same time, ambient air pressure and ambient air pressure with desiccant (supersaturated potassium carbonate solution).

The $\Delta H_{\mathrm{equ}}$ of water in aerogels can be estimated vaporizing the water with identical power input ($U_{\mathrm{in}}$), which has[1–5]

$$U_{in} = \Delta H_{vap} m_0 = \Delta H_{equ} m_g \tag{2}$$

where $\Delta H_{\mathrm{vap}}$ and $m_0$ were the evaporation enthalpy and mass change of bulk water; $m_g$ was the mass change of aerogel. The energy efficient was also calculated based on $E_{\mathrm{equ}}$

of corresponding aerogels. The water evaporation rate ratio and the corresponding calculated $H_{\mathrm{equ}}$ are shown in Fig. S4 and S5.

The experimental data of solar steam generation are based on the dark evaporation data and the specific calculation formula as follows:

$$\eta = \frac{\dot{m} H_{equ}}{C_{opt} P_0} \tag{3}$$

in which $\dot{m}$ is the mass flux, $H_{\mathrm{equ}}$ is the vaporization enthalpy of the water in the GO/maize straw aerogel, $P_0$ is the solar irradiation power of one sun (1 kW $m^{-2}$), and $C_{\mathrm{opt}}$ refers to the optical concentration on the absorber surface.

## 2 Supplemental Video S1-S3

**Video S1**

The wettability of the aerogel surface is achieved by dripping Congo red stained water

**Video S2**

Compressibility and resilience of aerogel

**Video S3**

Evaporation performance of aerogel on Congo red dyed emulsified oil

**Video S4**

The wettability of the GMN aerogel

## 3 Supplementary Figure

### 3.1 Relative materials and data

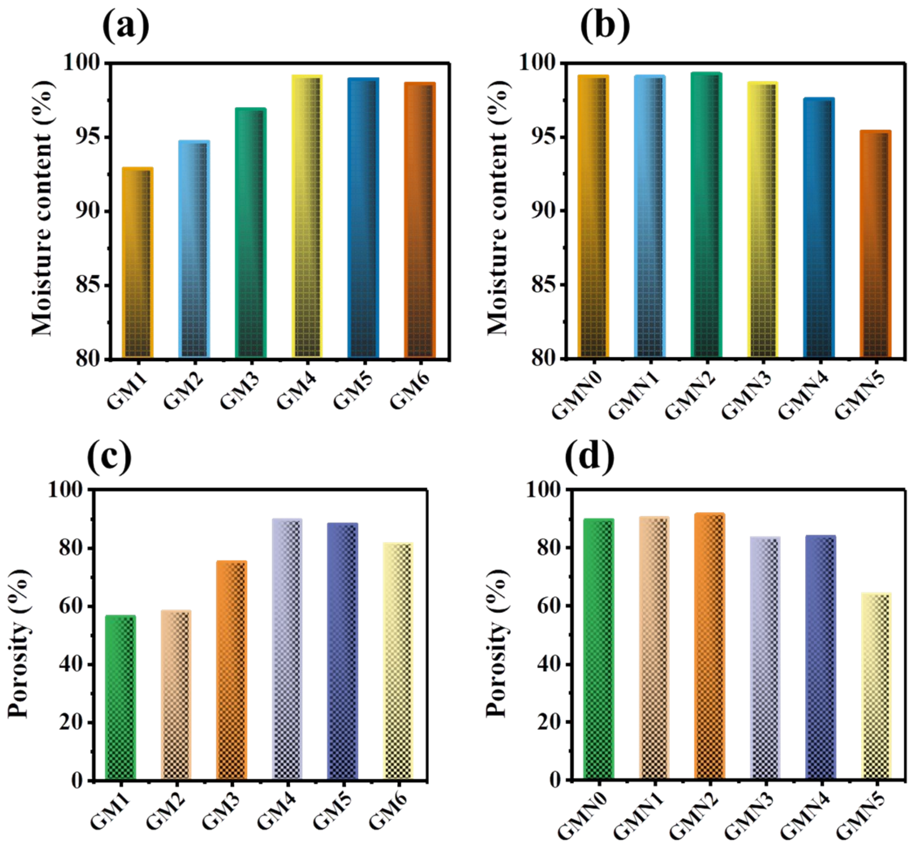

**Figure S1. (a) Moisture content of 3D-maize straw/GO hydrogels with different maize straw /GO ratios, (b) moisture content of 3D N-doped maize straw/GO hydrogels with different urea content, (c) the porosity of 3D-maize straw/GO aerogels with different maize straw /GO ratios, (d) the porosity of 3D N-doped maize straw/GO hydrogels with different urea content.**

**The porosity is calculated based on the followed equation:**

$$\varepsilon = \frac{\frac{m_2 - m_1}{\rho}}{\pi r^2 h} \quad (4)$$

where ε represent the porosity, ρ is the soaking medium solution density, $m_1$ is the mass of aerogel in the dry state, $m_2$ is the mass of an aerogel soaked to saturation.

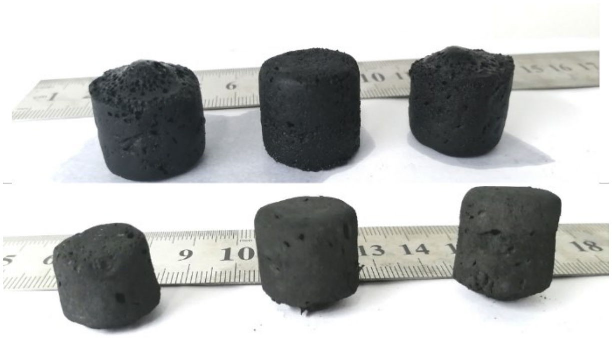

Figure S2. Optical images of hydrogels and aerogels for GMN2 (the hydrogel does not significantly shrink after atmospheric drying).

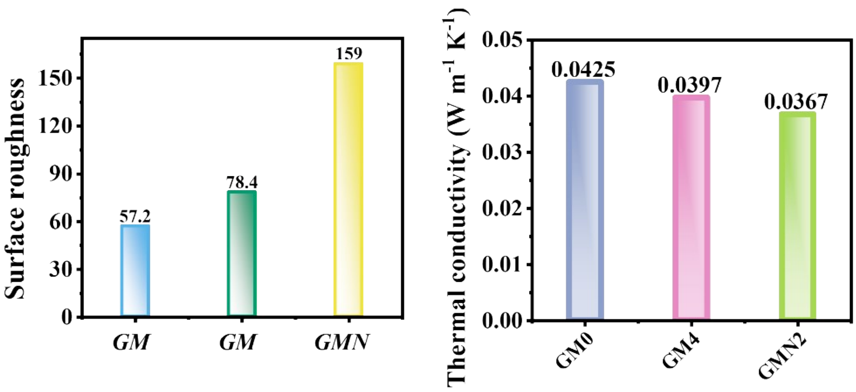

Figure S3. (a) Roughness of aerogel, (b)thermal conductivity of aerogel

## 3.2. Evaporation experiment

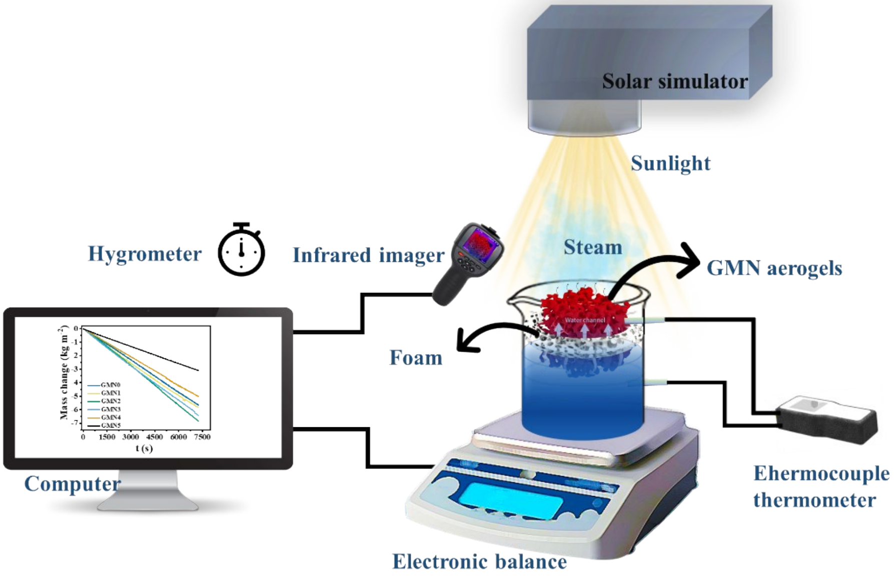

**Figure S4. The schematic diagram of the measurement system.**

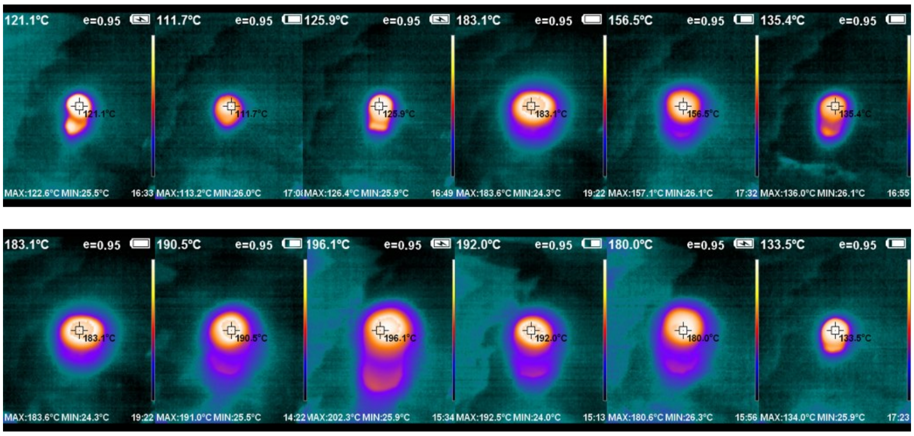

**Figure S5. Infrared thermal images of aerogels under 5 sun solar radiation.**

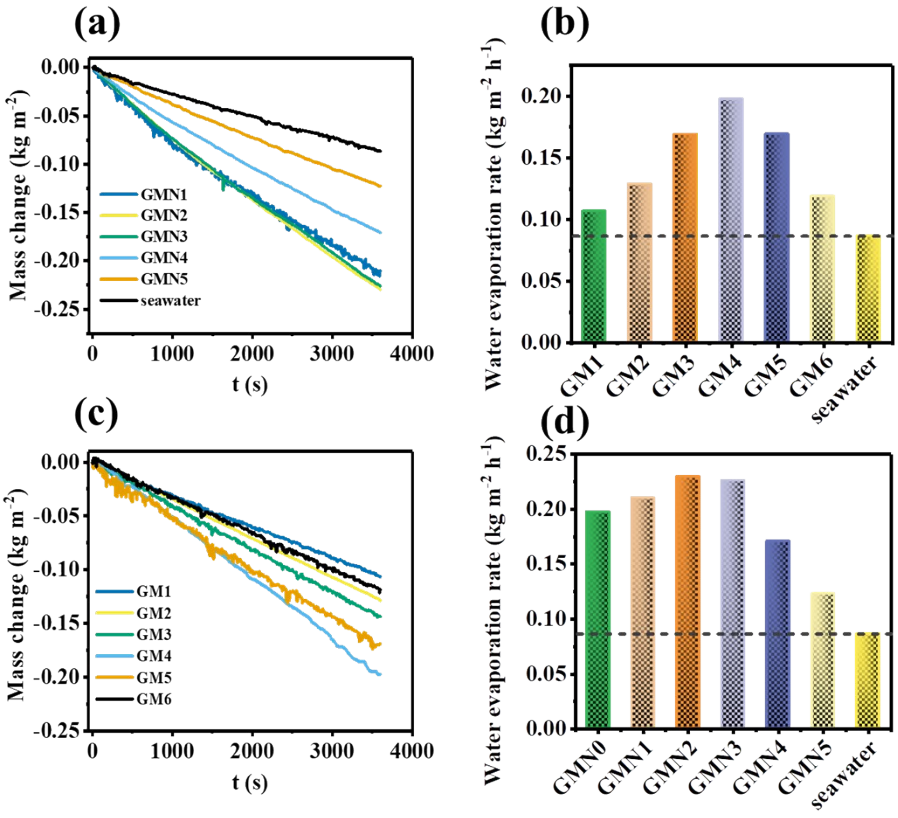

**Figure S6. (a) and (b) Time-dependent water mass change and water evaporation rates of 3D-maize straw/GO aerogels with different maize straw /GO ratios under dark circumstances, (c) and (d)time-dependent water mass change and water evaporation rates of 3D N-doped maize straw/GO aerogels**

**with different urea under dark circumstances. (the ambient temperature is 26 °C**

**and**

**the humidity is 45).**

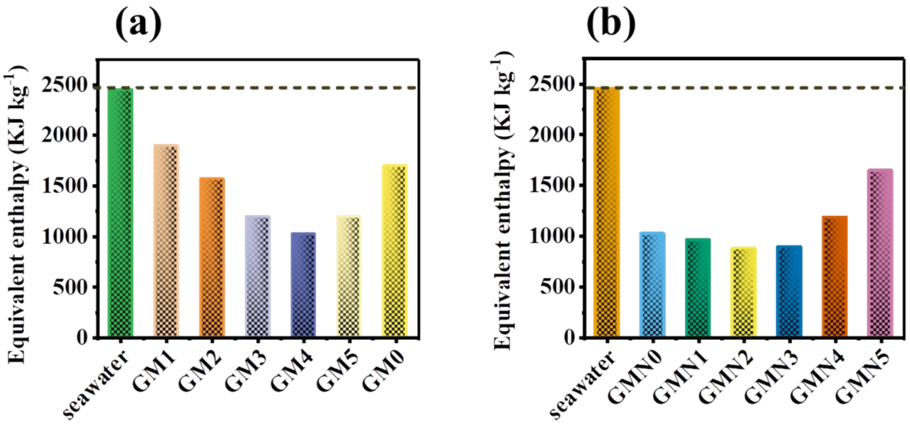

**Figure S7. (a) Calculated equivalent enthalpy of 3D-maize straw/GO aerogels with different maize straw /GO ratios, (b) calculated equivalent enthalpy of 3D N-doped maize straw/GO aerogels with different urea.**

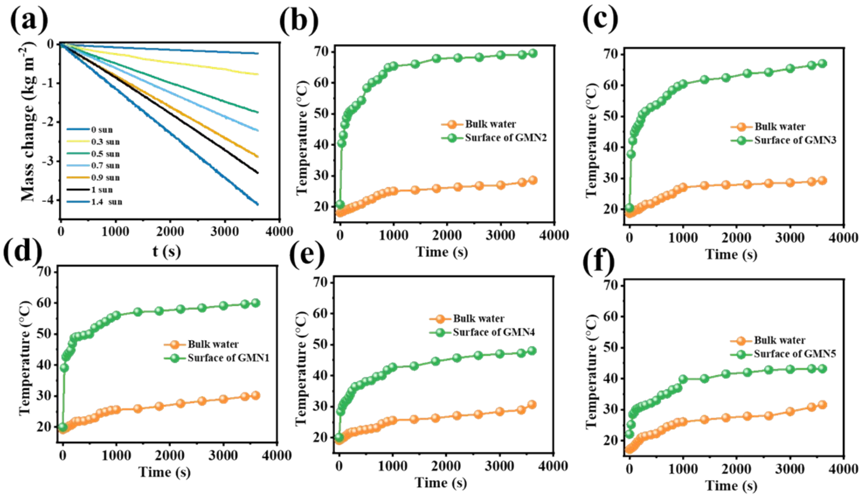

**Figure S8.** **(a) Time-dependent water mass change of different 3D-N-doped Maize straw/GO aerogels under different solar intensity, (b-f) time-dependent temperature of GMN and bulk water under 1sun.**

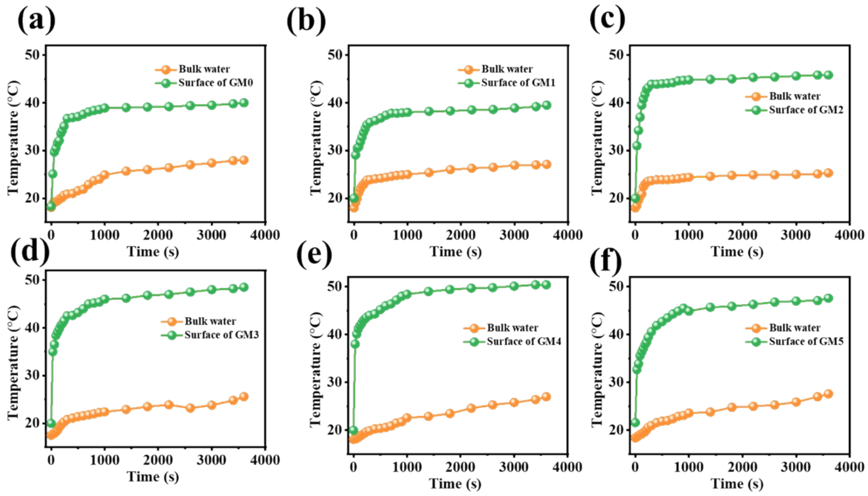

**Figure S9. (a-f) time-dependent temperature of GM and bulk water under 1sun.**

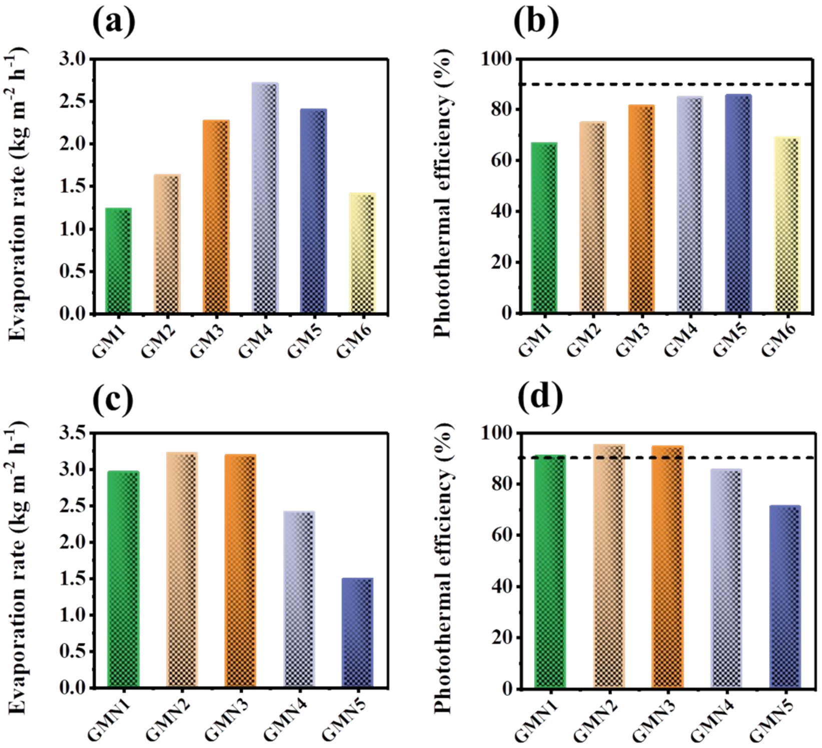

**Figure S10. (a) and (b) Evaporation rate and photothermal efficiency of the 3D-maize straw/GO aerogels with different maize straw /GO ratios, (c) and (d) evaporation rate and photothermal efficiency of 3D N-doped maize straw/GO aerogels with different urea.**

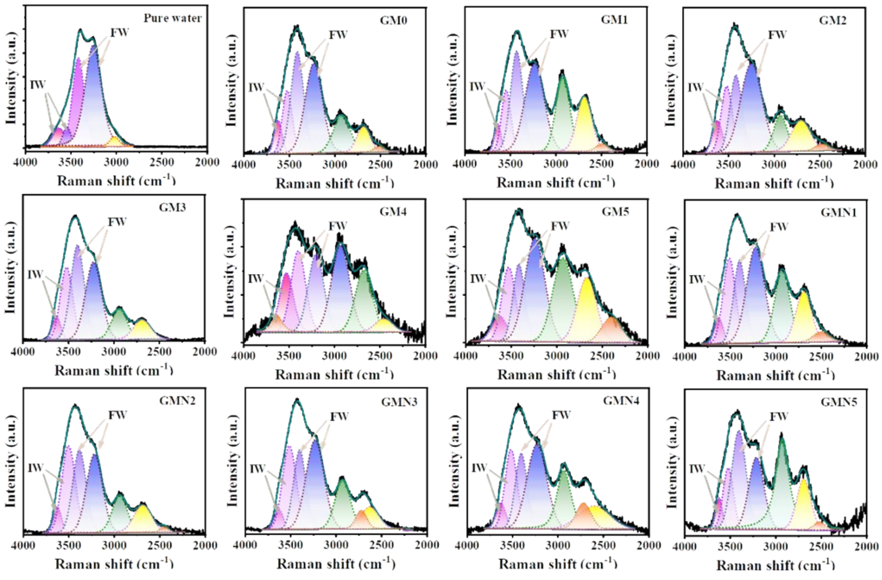

**Figure S11. Fitting curves in energy region O-H stretching modes for pure water, GM and GMN.**

We analyzed the existence of different water molecules in the aerogel after soaking by Raman spectroscopy, and the test result is shown in Figure S11. The Raman spectra of water, GM, and GMN were fitted by four peaks through Gaussian function, which are peaks observed at ~3239, 3414, 3529, and 3630 $cm^{-1}$. The peaks at 3233 $cm^{-1}$ and 3401$cm^{-1}$ are in-phase and out-of-phase O–H stretching vibration of free water molecules (FW) with four hydrogen bonds, while the peaks at 3514 $cm^{-1}$ and 3630 $cm^{-1}$ are related to the O–H symmetric and asymmetric stretching modes of weakly hydrogen bonded intermediate water molecules (IW). The results show that the ratios of intermediate water (IW): free water (FW) in pure water and pure graphene aerogel (GM0) are 0.13 and 0.30, respectively. For maize straw/graphene aerogels, the ratio of IW: FW in GM1, GM2, GM3, GM4, GM5 is 0.25, 0.38, 0.43, 0.47, 0.46, and 0.46, respectively. For N-doped maize straw/graphene aerogels, the ratios of IW:FW in GMN1, GMN2, GMN3, GMN4, and GMN5 are 0.48, 0.59, 0.51, 0.47, and 0.32, respectively. The results show that most of the water absorbed in the aerogel is weakly hydrogen bonded intermediate water, especially the nitrogen-doped aerogel GMN2. Therefore, the DSC of the aerogel after absorbing water was tested to further calculate the enthalpy of evaporation of the aerogel in water evaporation.

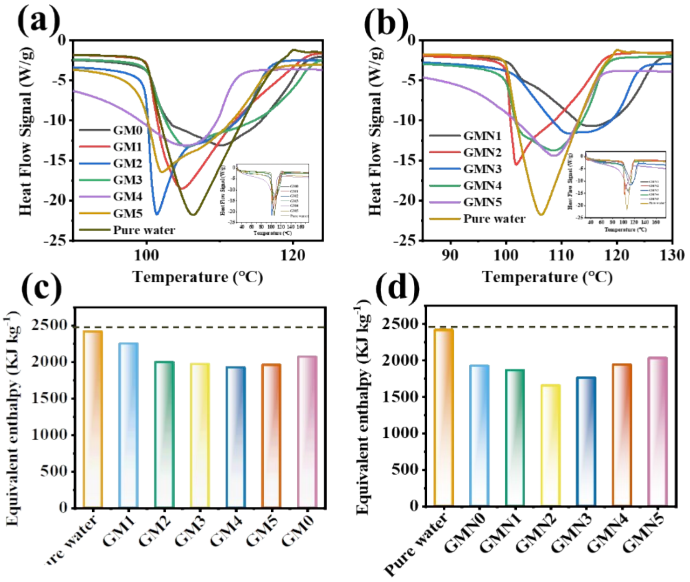

**Figure S12. DSC analysis of (a) GM and (b) GMN, enthalpy of evaporation calculated by DSC for (c) GM and (d)GMN.**

To measure the enthalpy of vaporization, the aerogel containing water is placed in an aluminum crucible fitted with a lid that is perforated by a laser through holes of 50 μm, so that the water vapor is diffused out by boiling at 100°C instead of nitrogen purging cause the evaporation of water vapor, and the measurement is performed at a linear heating rate of 5 ℃/min under a nitrogen flow (20 mL/min), in the temperature range from 30 to 180 ℃. The DSC curves of pure water, pure graphene aerogel (GM0), maize straw/graphene aerogels (GM), N-doped maize straw/graphene aerogels (GMN) and the calculated enthalpy of evaporation of water are shown in Figure S12. The results show that the peak width of aerogel is much wider than that of pure water, and the heat flow signal increases gradually after the signal reaches its minimum value, indicating that the water structure in aerogel is different from that of pure water, so the water evaporation process is also different. The evaporation enthalpy of pure water and aerogel is calculated, and it is found that the evaporation enthalpy of pure water is 2417 KJ $kg^{-1}$., which is close to the theoretical value of 2444 KJ $kg^{-1}$. Due to the influence of the three-dimensional network structure on the evaporation process, the evaporation enthalpy of aerogel is much smaller, especially the evaporation enthalpy of GMN2 is as low as 1659 KJ $kg^{-1}$. In addition, the enthalpy of evaporation calculated by DSC is higher than the enthalpy of evaporation test due to DSC is completely dehydrated while evaporation test is a slightly dehydrated process.

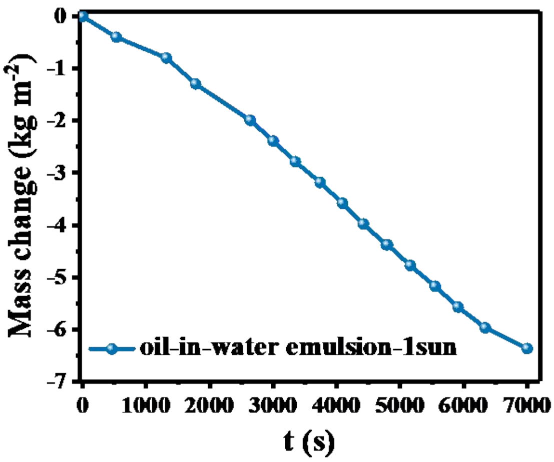

**Figure S13 Time-dependent water mass change of GMN2 aerogels immersion in oil-in-water emulsion under 1 sun**

### 3.3. The Cost efficiency analysis

The total cost of aerogel used for solar-driven water evaporation is composed of labor costs, equipment costs, material costs, and seawater treatment costs. Due to differences in labor costs and equipment costs in various regions, it is not considered. In addition, solar-powered water evaporation can be considered cost-free in terms of seawater treatment. Therefore, the discussion here focuses on the cost of aerogel materials. Take the synthesis of a batch of GMN aerogel as an example to calculate the cost. The production of a synthetic batch of GMN2 was approximately 3 quantities of aerogels with a diameter of 2cm and a height of 2cm. The cost is as follows:

**Table S1. The Cost efficiency analysis.**

| Type | | Price | Cost ($) |
|---|---|---|---|
| Materials | graphite oxide | 448.80 $/kg | 0.03366 |
| | Urea | 5.08 $/kg | 0.0025432 |
| | Ascorbic acid | 3.88 $/kg | 0.0019448 |
| | SDS | 0.30 $/kg | 0.00002992 |
| | Maize Straw | Free | 0 |

| | | | |
|---|---|---|---|
| Others | Power fare | 89.76 \$/(Kw·h) | 0.2992 |
| | Water rate | 0.30 \$/L | 0.004488 |
| Total | | | 0.34 |

It will cost about 0.12 \$ to produce a GMN2 aerogel with a diameter of 2 cm and a height of 2 cm.

## 3.4 Comparing with others in literatures

**Table S2. Comparison of the evaporation process described in the literature.**

| Materials | Evaporation efficiency and rate under 1 sun | Efficiency | Control measures for heat-to-vapor conversion | Ref. |
|---|---|---|---|---|
| Cu nanoparticles combining the carbon-decorated TiO2 | 1.5<br>kg $m^{-2}$ $h^{-1}$ | 92.2% | The wrinkled surfaces and inter-particle voids provide large interfacial areas and unique micro-channels | 6 |
| Porous N-doped graphene | 1.50<br>kg $m^{-2}$ $h^{-1}$ | 80% | The porous graphene by optimizing specific heat, light absorption, thermal conductivity, and water capillary through morphology design and physical property tuning | 7 |
| 3D cross-linked honeycomb graphene foam | 2.6<br>kg $h^{-1}$ $m^{-2}$ $g^{-1}$ | ~87% | (1) the ultralow density and low thermal conductivity prevent the heat conduction to the underlying and surrounding water.<br>(2) hydrophilicity and porous structure cause an automatic water transport | 8 |
| Layer-by-layer 3D-printed evaporator (CNT/GO, GO/NFC layer, and GO/NFC wall) | 1.25<br>kg $m^{-2}$ $h^{-1}$ | 85.6% | The 3D-printed porous concave structure has a high light-thermal conversion efficiency and intrinsic low thermal conductivity, which contributes to heat localization and alleviating thermal dissipation. | 9 |
| Modified graphene aerogel | - | 76.9% | Low thermal conductivity and abundant pore structure | 10 |
| RGO-agarose-cotton aerogel | 4.0<br>kg $m^{-2}$ $h^{-1}$ | 133%–139% | The net energy gain from the environment and the stored water through the cool side walls with large surface areas, and the cessation of heat conduction loss | 11 |

| | | | | |
|---|---|---|---|---|
| Carbon-coated paper (CP) on polystyrene foam | 2.20 kg m $^{-2}$ h $^{-1}$ | 120.7% | The total vapor generation rate is higher than the upper limit that can be produced by the input solar energy because of extra energy taken from the warmer environment | 12 |
| 3D cup-shaped photothermal structure (20 mixed metal oxide-type inorganic pigments) | 2.04 kg m $^{-2}$ h $^{-1}$ | 100% | (1) The inner wall gains energy by recovering the diffuse reflected light and thermal radiation from the bottom part<br>(2) Additional heat was gained from the ambient air when the 3D structure | 13 |
| Poly(vinyl alcohol) and activated carbon | 2.6 kg m $^{-2}$ h $^{-1}$ | ∽91% | Enhancing solar vapor generation by tailoring surface topography | 14 |
| CNTs/BC/GBs/wood | 2.9 kg m $^{-2}$ h $^{-1}$ | 80% | The high light absorbance, effective thermal management, fast water transportation, and reduced vaporization enthalpy. | 15 |
| Nitric acid immersion method to treat commercial black sponges | 2.72 kg m $^{-2}$ h $^{-1}$ | - | The size of water droplet can be reduced to a nanoscale size through the superhydrophilic sponge, resulting in the reduction of latent heat of water evaporation | 16 |
| $Fe_3Si$ aerogel supported on melamine foam | 2.08 kg m $^{-2}$ h $^{-1}$ | 91.8% | Outstanding anti-corrosion ability, full sunlight absorption (up to 2400 nm), low thermal conductivity (0.04 W m $^{-1}$ K $^{-1}$) and the ability to reduce the latent heat of water evaporation. | 2 |
| Patchy-surface hydrogel | 4.0 kg m $^{-2}$ h $^{-1}$ | 93% | (1) Hydrophilic hydrogel evaporators with hydrophobic island-shaped patches<br>(2) The increased thickness of the water layer in the hydrophilic region leads to the rapid escape of water molecules, while relatively long contact lines promise considerable water evaporation from the hydrophobic region | 4 |
| 3D $Ni_1Co_3$@PDA-based photothermal sponges | 2.42 kg m $^{-2}$ h $^{-1}$ | 109% | The eliminated heat conduction loss, reduced radiation and convection loss, as well as net energy gain from the environment | 17 |
| RGO coated cellulose sponge | 4.35 kg m $^{-2}$ h $^{-1}$ | 185.9% | Under 1.0 sun, the temperature of all the evaporation surfaces of the 3D spiral evaporator were lower than the environmental temperature, thus completely eliminated the energy loss and in turn gained energy from the environment and bulk water. | 18 |
| RGO-cotton | 2.95 kg m $^{-2}$ h $^{-1}$ | - | Cold evaporation surface between the solar evaporation surface and bulk water can extract energy from both sides. | 19 |

**Table S3 Comparison of carbon-based aerogel materials for water evaporation**

| Materials | Evaporation efficiency and rate under 1 sun | Solar absorbance | Structural design | Material advantages | Ref. |
|---|---|---|---|---|---|
| $CNTs@SiO_2$ nanofibrous aerogels | 1.50 kg $m^{-2}$ $h^{-1}$ | 98% (200-2500 nm) | Vertically aligned vessels and porous vessel walls | Excellent salt transportation performance from high to low salinity brine along the vessels or through the pores on vessel walls | 20 |
| Structure-guided wood aerogel | 1.35 kg $m^{-2}$ $h^{-1}$<br>90.89% | favorable light absorption (200–2500 nm) | natural aligned cellulose fibers provide capillary low-touristy channels with a hydrophilic surface | (1) Dynamically form the available air–water interface.<br>(2) Avoid the heat loss<br>(3) The temperature gradient formed would force natural convection and thus promote the evaporation efficiency | 21 |
| Graphene and rice-straw-fiber-based aerogels | 2.25 kg $m^{-2}$ $h^{-1}$<br>88.9% | 96–97% (200–2500 nm) | (1) rice straw cellulose as skeleton improves mechanical stability and flexibility<br>(2) porous structure and superhydrophilicity | Increasing the height of the photothermal aerogel, decreased the temperature on both the top and side evaporation surfaces, leading to less radiation and convection loss with more energy gain from the surrounding environment | 22 |
| vertically aligned Au/N-doped reduced graphene oxide (N-RGO) aerogel | 2.72 kg $m^{-2}$ $h^{-1}$<br>97.1% | 99.7% (200–2500 nm) | (1) introducing gradient vertical-microchannels and integrating Au nanoparticles nearby nanopores<br>(2) vertically aligned Au/graphene meshes with confined heat at micro and nanoscale levels | (1) the unique vertical microchannels, the porous ring-like N-RGO aerogel exhibited enhanced photothermal conversion, rapid water capillary pumping to hot regions, and effective interfacial evaporation.<br>(2) plasmonic Au nanoparticles can both serve as powerful nano-heaters<br>(3) the environment also contributed to the efficient energy conversion. | 23 |

| | | | | | |
|---|---|---|---|---|---|
| Cellulose-conducting polymer aerogels | 1.61<br>kg m $^{-2}$ h $^{-1}$<br>81% | 99%<br>(200–2500 nm) | 2 mm thick aerogel is located on top of the steam generator to absorb and convert sunlight and provide a large evaporation internal surface | (1) porous structure provides a large interfacial surface area for water molecules to be evaporated from<br>(2) open porous structure forms pathway channels for water transport<br>(3) the heat localization for evaporation. | 24 |
| CS-based GO aerogel | 1.78<br>kg m $^{-2}$ h $^{-1}$ | 93%<br>(200–2500 nm) | (1) through liquid-phase one-pot freeze drying without any cross-linkers<br>(2) pore size and structure of the CS aerogel could be modulated by changing the freeze-drying technology. | integrated biocompatible, hydrophilic and high thermal insulation properties, as well as enhanced light absorption ability based on the designed porous structure through the effects of light trapping and multiple scattering | 25 |
| All-nanofiber aerogel | 1.11<br>kg m $^{-2}$ h $^{-1}$<br>76.3% | 97.5%<br>(200–2500 nm) | assembled into a 3D porous aerogel structure with excellent structural integrity and resilience | thermal-localization and management capabilities using this bilayer structure | 26 |
| RGO-SA-CNT aerogels | 1.622<br>kg m $^{-2}$ h $^{-1}$<br>83% | 92%<br>(200–2500 nm) | (1) introduced multiwalled carbon nanotubes can enable efficient solar absorption.<br>(2) good hydrophilicity and porous networks | The efficient absorption across the full solar spectrum, good wettability, together with the porous structure which enables efficient water supply and vapor channel and very low thermal conductivity make RGO-SA-CNT aerogels ideal absorbers for solar steam generation. | 27 |
| Conjugated microporous polymers aerogels | 86.8% | 99%<br>(200–2500 nm) | simple carbonization of the as-formed carbon-rich tubular CMPs aerogels precursors to obtain conjugated microporous polymer carbon aerogels (CMPCAs) | the surface modification of the resulting monolithic carbon aerogels makes them superhydrophilic which facilitate the rapid transportation of water molecules. | 28 |

| | | | | | |
|---|---|---|---|---|---|
| $MnO_2$ nanowire –reduced graphene oxide monolithic aerogels | 1.587 kg m $^{-2}$ h $^{-1}$<br>93.8% | 100% (200–2500 nm) | $MnO_2$ nanowire-reduced graphene oxide aerogels coated with polypyrrole | PNGAs possess superhydrophilic wettability which facilitates rapid transportation for water molecules. strong light absorption performance, superhydrophilic surface wettability, interpenetrated porous architecture and excellent thermal insulation | 29 |
| Nanofibrous Aerogels | 2.89 kg m $^{-2}$ h $^{-1}$<br>90.3% | 98.9% (200–2500 nm) | blending the random copolymer of polyvinyl alcohol and polyethylene (PVA-*co*-PE) with zirconium carbide (ZrC) nanoparticles (NPs) | highly porous structure with vertically aligned microchannels and microsized pores distributed on the walls of aerogels could facilitate the enhancement of water transportation | 30 |
| D-$HNb_3O_8$/PAM aerogels | 1.401 kg m $^{-2}$ h $^{-1}$<br>91% | 90% (200–2500 nm) | (1) the D-$HNb_3O_8$ absorbs the full solar spectrum<br>(2) the hydrophilic PAM chains form an interconnected thermal insulation porous structure with capillary pumping capability | (1) the harvested and converted solar energy over D-$HNb_3O_8$ can be directly delivered to the captured molecules absorbed on the PAM chains and water confined in the molecular meshes<br>(2) PAM chains can minimize heat loss and supply adequate water for continuous solar vapor generation | 31 |
| N-doped reduced graphene oxide 3D aerogels | 2.53 kg m $^{-2}$ h $^{-1}$<br>90.3% | 74.8% (200–2500 nm) | gradient microchannels are constructed by introducing a concentration gradient of $NH_4OH$ within the N-RGO hydrogel before traditional freeze-drying | unique 3D gradient vertical microchannels concentrate water into hot regions and achieve effective interfacial evaporation | 32 |
| 3D nitrogen-doped graphene/carbon hybrid aerogel (NGCA) | 1.558 kg m $^{-2}$ h $^{-1}$<br>90% | 97.57% (200–2500 nm) | prepared NGCA composites by repeated dip-coating, air-drying and high-temperature carbonization processes | excellent absorption of solar spectrum, good hydrophilicity, porous networks for efficient water supply and vapor channels, and thermal insulating property for heat localization. | 33 |

## Supplemental References

1 X. Bai, Y. Li, F. Zhang, Y. Xu, S. Wang and G. Fu, *Environ. Sci. Water Res. Technol.*, 2019, **5**, 2041–2047.

2 F. Zhang, Y. Li, X. Bai, S. Wang, B. Liang, G. Fu and Z. S. Wu, *J. Mater. Chem. A*, 2018, **6**, 23263–23269.

3 Y. Li, M. Zhao, Y. Xu, L. Chen, T. Jiang, W. Jiang, S. Yang and Y. Wang, *J. Mater. Chem. A*, 2019, **7**, 26769–26775.

4 Y. Guo, X. Zhao, F. Zhao, Z. Jiao, X. Zhou and G. Yu, *Energy Environ. Sci.*, , DOI:10.1039/d0ee00399a.

5 F. Zhao, X. Zhou, Y. Shi, X. Qian, M. Alexander, X. Zhao, S. Mendez, R. Yang, L. Qu and G. Yu, *Nat. Nanotechnol.*, 2018, **13**, 489–495.

6 X. Zhang, X. Wang, W. D. Wu, X. D. Chen and Z. Wu, *J. Mater. Chem. A*, 2019, **7**, 6963–6971.

7 Y. Ito, Y. Tanabe, J. Han, T. Fujita, K. Tanigaki and M. Chen, *Adv. Mater.*, 2015, **27**, 4302–4307.

8 Y. Yang, R. Zhao, T. Zhang, K. Zhao, P. Xiao, Y. Ma, P. M. Ajayan, G. Shi and Y. Chen, *ACS Nano*, 2018, **12**, 829–835.

9 Y. Li, T. Gao, Z. Yang, C. Chen, W. Luo, J. Song, E. Hitz, C. Jia, Y. Zhou, B. Liu, B. Yang and L. Hu, *Adv. Mater.*, 2017, **29**, 1700981.

10 Y. Fu, G. Wang, X. Ming, X. Liu, B. Hou, T. Mei, J. Li, J. Wang and X. Wang, *Carbon N. Y.*, 2018, **130**, 250–256.

11 X. Wu, T. Gao, C. Han, J. Xu, G. Owens and H. Xu, *Sci. Bull.*, 2019, **64**, 1625–1633.

12 H. Song, Y. Liu, Z. Liu, M. H. Singer, C. Li, A. R. Cheney, D. Ji, L. Zhou, N. Zhang, X. Zeng, Z. Bei, Z. Yu, S. Jiang and Q. Gan, *Adv. Sci.*, 2018, **5**, 1800222.

13 Y. Shi, R. Li, Y. Jin, S. Zhuo, L. Shi, J. Chang, S. Hong, K.-C. Ng and P. Wang, *Joule*, 2018, **2**, 1171–1186.

14 X. Hu, W. Xu, L. Zhou, Y. Tan, Y. Wang, S. Zhu and J. Zhu, *Adv. Mater.*, 2017, **29**, 1604031.

15 Q. F. Guan, Z. M. Han, Z. C. Ling, H. Bin Yang and S. H. Yu, *Nano Lett.*, 2020, **20**, 5699–5704.

16 X. Bai, Y. Li, F. Zhang, Y. Xu, S. Wang and G. Fu, *Environ. Sci. Water Res. Technol.*, 2019, **5**, 2041–2047.

17 B. Shao, Y. Wang, X. Wu, Y. Lu, X. Yang, G. Y. Chen, G. Owens and H. Xu, *J. Mater. Chem. A*, 2020, **8**, 11665–11673.

18 Y. Wang, X. Wu, T. Gao, Y. Lu, X. Yang, G. Y. Chen, G. Owens and H. Xu, *Nano Energy*, 2020, 105477.

19 Y. Wang, X. Wu, X. Yang, G. Owens and H. Xu, *Nano Energy*, 2020, **78**, 105269.

20 X. Dong, L. Cao, Y. Si, B. Ding and H. Deng, *Adv. Mater.*, 2020, **32**, 1–8.

21 W. Chao, X. Sun, Y. Li, G. Cao, R. Wang, C. Wang and S. H. Ho, *ACS Appl. Mater. Interfaces*, 2020, **12**, 22387–22397.

22 D. P. Storer, J. L. Phelps, X. Wu, G. Owens, N. I. Khan and H. Xu, *ACS Appl. Mater. Interfaces*, 2020, **12**, 15279–15287.

23 X. Meng, J. Yang, S. Ramakrishna, Y. Sun and Y. Dai, *J. Mater. Chem. A*, 2020, **8**, 16570–16581.

24 S. Han, T. P. Ruoko, J. Gladisch, J. Erlandsson, L. Wågberg, X. Crispin and S. Fabiano, *Adv. Sustain. Syst.*, , DOI:10.1002/adsu.202000004.

25 Y. Gu, X. Mu, P. Wang, X. Wang, J. Liu, J. Shi, A. Wei, Y. Tian, G. Zhu, H. Xu, J. Zhou and L. Miao, *Nano Energy*, 2020, **74**, 104857.

26 F. Jiang, H. Liu, Y. Li, Y. Kuang, X. Xu, C. Chen, H. Huang, C. Jia, X. Zhao, E. Hitz, Y. Zhou, R. Yang, L. Cui and L. Hu, 2019, **9**, 1802158.

27 X. Hu, W. Xu, L. Zhou, Y. Tan, Y. Wang and S. Zhu, *Adv. Mater.*, 2017, **29**, 1604031.

28 P. Mu, Z. Zhang, W. Bai, J. He, H. Sun, Z. Zhu, W. Liang and A. Li, *Adv. Energy Mater.*, 2019, **9**, 1802158.

29 Z. Zhang, P. Mu, J. Han, J. He, Z. Zhu, H. Sun, W. Liang and A. Li, *J. Mater. Chem. A*, 2019, **7**, 18092–18099.

30 T. Mei, J. Chen, Q. Zhao and D. Wang, *ACS Appl. Mater. Interfaces*, 2020, **12**, 42686–42695.

31 M.-Q. Yang, C. F. Tan, W. Lu, K. Zeng and G. W. Ho, *Adv. Funct. Mater.*, 2020, **30**, 2004460.

32 X. Meng, J. Yang, S. Ramakrishna, Y. Sun and Y. Dai, *ACS Sustain. Chem. Eng.*, 2020, **8**, 4955–4965.

33 B. Huo, D. Jiang, X. Cao, H. Liang, Z. Liu, C. Li and J. Liu, *Carbon N. Y.*, 2019, **142**, 13–19.